Towards Pareto optimal high entropy hydrides via data-driven materials discovery

Matthew Witman, Sanliang Ling, Matthew Wadge, Anis Bouzidi, Nayely Pineda-Romero, Rebecca Clulow, Gustav Ek, Jeffery Chames, Emily Allendorf, Sapan Agarwal, et al.

Towards Pareto optimal high entropy hydrides via data-driven materials discovery

Matthew D. Witman,[*,†] Sanliang Ling,[‡] Matthew Wadge,[‡] Anis Bouzidi,[¶] Nayely Pineda-Romero,[¶] Rebecca Clulow,[§] Gustav Ek,[§] Jeffery M. Chames,[†] Emily J. Allendorf,[†] Sapan Agarwal,[†] Mark D. Allendorf,[†] Gavin S. Walker,[‡] David M. Grant,[‡] Martin Sahlberg,[§] Claudia Zlotea,[¶] and Vitalie Stavila[*,†]

†*Sandia National Laboratories, Livermore, California 94551, United States*
‡*Advanced Materials Research Group, Faculty of Engineering, University of Nottingham, University Park, Nottingham, NG7 2RD, UK*
¶*Univ Paris Est Créteil, CNRS, ICMPE, UMR 7182, 2 rue Henri Dunant, 94320, Thiais, France*
§*Department of Chemistry - Ångström Laboratory, Uppsala University, Box 523, SE-75120, Uppsala, Sweden*

E-mail: mwitman@sandia.gov; vnstavi@sandia.gov

Abstract

The ability to rapidly screen material performance in the vast space of high entropy alloys is of critical importance to efficiently identify optimal hydride candidates for various use cases. Given the prohibitive complexity of first principles simulations and large-scale sampling required to rigorously predict hydrogen equilibrium in these systems, we turn to compositional machine learning models as the most feasible approach to screen on the order of tens of thousands of candidate equimolar alloys. Critically, we show that machine learning models can predict hydride thermodynamics and capacities with reasonable accuracy (e.g. a mean absolute error in desorption enthalpy prediction of $\sim$5 kJ/molH_2) and that explainability analyses capture the competing trade-offs that arise from feature interdependence. We can therefore elucidate the multi-dimensional Pareto optimal set of materials, i.e., where two or more competing objective properties can't be simultaneously improved by another material. This provides rapid and efficient down-selection of the highest priority candidates for more time-consuming density functional theory investigations and experimental validation. Various targets were selected from the predicted Pareto front (with saturation capacities approaching two hydrogen per metal and desorption enthalpy less than 60 kJ/molH_2) and were experimentally synthesized, characterized, and tested amongst an international collaboration group to validate the proposed novel hydrides. Additional top-predicted candidates are suggested to the community for future synthesis efforts, and we conclude with an outlook on improving the current approach for the next generation of computational HEA hydride discovery efforts.

Introduction

Hydrogen is a promising energy carrier that has significant potential to decarbonize economic sectors that produce "difficult-to-abate" emissions, including heavy duty transportation (maritime shipping, rail, long-haul trucks), aviation, high temperature industrial applications (chemicals, steel making), and seasonal grid storage.[1] Yet the lack of the demonstrated com-

mercial progress to-date mainly stems from significant technical challenges related to the storage, transportation, and generation of green hydrogen.[2,3] In terms of hydrogen storage, intermetallic compounds and their substituted alloys have long been studied as promising candidates because they achieve hydrogen volumetric densities on par with or exceeding compressed gas (e.g., 700 bar H_2) at significantly lower pressures.[4–11] While lighter weight complex hydrides have been intensively investigated in the context of light duty vehicle applications,[12,13] high performance but heavier metal alloy-based hydrides could be attractive in stationary applications where weight of the hydride bed is of less concern, i.e. stationary and seasonal grid storage and hydrogen compression.[14–17]

While exploration of intermetallic and alloy hydrides in novel structural/chemical space has traditionally been an intuitive process and guided by manually derived design rules and thermodynamic models (see Ref. 18 and references therein), recent years have also seen a "big-data" approach to hydride discovery. These span various applications and approaches: from deep learning methods for predicting superconducting hydrides[19] or resolving hydride location in metal nanoclusters[20] to tree-based models to predict metal hydride thermodynamics for hydrogen compressor materials.[21] Compositional machine learning models[22–24] have also been trained on experimentally collected hydride thermodynamic data,[25] then applied to high-throughput screening novel composition spaces to search for possible materials exhibiting desired hydride thermodynamics.[26] This efficient modeling capability becomes increasingly necessary when considering hydrides based on high entropy alloys (HEAs),[27,28] a relatively nascent class of hydrides[29] first highlighted for their outstanding volumetric capacities arising from exceptionally large hydrogen to metal (H/M) ratios.[30] The combinatorial explosion of compositional design space in equimolar HEAs alone is simply too large for brute-force experimental search[31] or modeling with compute-intensive methods like density functional theory (DFT). While experimental validation of ML-predicted hydride thermodynamics has indeed been demonstrated,[26,32] and the space of experimentally investigated HEA hydrides is ever growing,[33–39] only a small fraction of possible compositional space has been explored. Furthermore, a perspective on the possible upper bounds of HEA hydride performance remains elusive.

To address some of these opportunities and further drive discovery with data-driven methods, we first improve upon our previously developed hydride thermodynamic models. v0.0.4 of the ML-HydPARK training database[40] was augmented to contain additional HEA hydride thermodynamic properties from literature studies when the necessary pressure-composition-temperature (PCT) measurements were performed to extract the enthalpy and entropy of hydrogen desorption (ΔH and ΔS) and saturation capacity (H/M).[26,30,32,35,37,41] Thermodynamic properties from metal hydrides investigated for hydrogen compression were also added to the training data.[15] We then expanded the scope of these models over our previous work by predicting new properties like H/M. Explainability analyses[42,43] of these models importantly reveal the interdependence of different thermodynamic properties on the same material features, which leads to unavoidable and well-known trends in hydride design, i.e. the enthalpy-capacity trade-off or the enthalpy-entropy correlation effect. These represent competing objectives that are detrimental for most proposed use cases of hydrides, e.g., reducing the desorption enthalpy of high capacity hydrides reduces the required desorption temperature but typically also reduces the capacity. When such competing objectives exist, one seeks the Pareto optimal set of candidates among all possible materials: candidates where no further improvement of one objective (minimizing desorption enthalpy) can be achieved without penalizing another objective (maximizing capacity). After screening tens of thousands of HEA candidate compositions with the ML models, a multi-objective Pareto optimal front of just tens of materials can be ascertained.

Finally, predicted Pareto (or near Pareto) optimal materials were selected for experimental validation. Target HEA compositions were

also selected to be similar to previously synthesized compounds, yet different enough to challenge the ML-prediction task. In the end, Mg containing compositions were selected for experimental validation (MgAlTiVCr, MgTiVNbCr, and MgTiVZrNbHf), even though there are no Mg containing equimolar HEAs in the training data. ML-predictions and experiments are in good agreement, as well as the DFT calculations used to gain insight into mechanisms and thermodynamics of hydrogen absorption in these HEAs. This holistic validation of our data-driven approach to synthesizing predicted Pareto optimal materials serves as a blueprint for further hydride discovery, although there remains significant potential for further acceleration. Currently, the speed at which PCT measurements can be performed is a bottleneck to experimental data acquisition and model validation, especially when the kinetics of absorption and desorption are sluggish. Alternative methods could be explored in the future to facilitate faster experimental data acquisition.[31,44–46]

Methods

This section details (1) the experimental methods used for synthesizing, characterizing, and testing high entropy hydrides; (2) the methods for machine learning model training, validation, interpretability analysis, high-throughput screening, and Pareto optimality of HEA hydride candidates; and (3) the density functional theory methods for additionally understanding hydriding mechanisms and predicting the thermodynamic driving forces and high capacities in HEA hydrides.

Experiments

HEA synthesis. Due to the low melting temperature of Mg and Al and the high vapour pressure of Mg, the selected compositions were directly synthesized as hydride phases following a two-step procedure: first, pre-alloys of refractory elements were prepared by arc melting followed by reactive ball milling (RBM) of the pre-alloy with the Mg/Al in powder form under high H_2 pressure. The pre-alloys TiVCr, TiVCrNb and TiVZrNbHf were synthesized by arc melting under Ar atmosphere from lumps of Ti (Neyco, 99.99% metals basis), V (Neyco, 99.9% metals basis), Cr (Alfa Aesar, 99.99% metals basis), Zr (Neyco, 99.95% metals basis), Nb (Alfa Aesar, 99.95% metals basis) and Hf (Alfa Aesar, 99.9% metals basis). They were flipped and remelted 12 times to ensure chemical homogeneity. The pre-alloys were crushed in pieces by hammering and further used in the second step of the synthesis. The reactive ball milling of Mg (Alfa Aesar, 99.8% metals basis) and Al (Strem Chemicals, 99% metals basis) powders and the pre-alloy was performed under 70 bar H_2 pressure for 120 minutes process following the procedure reported elsewhere.[33] During the initial filling of the RBM vial with H_2 gas, the pre-alloys TiVCr and TiVCrNb spontaneously absorb hydrogen at room temperature forming hydrides. Thus, the hydrogen content in the final compositions MgAlTiVCr and MgTiVCrNb is calculated based on two separate reactions: the hydrogenation of the pre-alloy at room temperature and the hydrogen absorption during the RBM process. The TiVZrNbHf pre-alloy did not show any hydrogen absorption during the initial filling of the vial, in agreement with our previous results.[30] For this last sample, we have demonstrated the repeatability of the two-step synthesis by performing the same procedure several times and obtaining similar results in terms of both crystalline lattice of the hydride and its hydrogen content.

X-ray diffraction. Structural characterizations of the hydride phases after RBM were carried out by X-ray powder diffraction (XRD) using the laboratory D8 advance Bruker instrument (Cu K_α radiation $\lambda = 1.5406$ Å, Bragg-Brentano geometry) in a 2θ range from 10 to 90°.

Energy Dispersive X-Ray Spectroscopy. Scanning electron microscopy (SEM) and energy-dispersive spectroscopy (EDS) measurements on MgTiVZrNbHf, MgTiVCrNb and

MgAlTiVCr phases before and after hydrogen cycling were performed on a Jeol JSM-7600F thermal field emission scanning electron microscope equipped with an Oxford X-Max detector and operated at 10 and 15 kV. The samples were deposited onto aluminum stubs using double-sided carbon tape.

PCT data collection. The absorption pressure–composition–temperature (PCT) isotherm of MgTiVZrNbHf was collected on an automated PCTPro instrument from Setaram, which allows accurate volumetric determination of the amounts of hydrogen absorbed by the sample by using calibrated volumes. The pressure was monitored with high-accuracy pressure transducers while the sample was maintained at the desired temperature and dosed with hydrogen. Prior to PCT measurements, the samples were activated in vacuum at 653 K. The enthalpy and entropy of MgTiVZrNbHf hydrogenation were determined using a published hybrid PCT/van't Hoff method by measuring a full hydrogen isotherm at 644 K, then reducing the sample temperature to 633 and 621 K and re-measuring the equilibrium pressure.[26] The absorption PCT isotherm for the MgAlTiVCr phase was collected using an in-house built Sieverts apparatus following a similar methodology, with initial temperature of 653 K, then repeating hydrogenation measurements at 673 and 693 K to re-measure equilibrium pressure. Three absorption PCT isotherms for the MgTiVCrNb were collected at 644, 654 and 664 K after activation in vacuum at 683 K via an in-house built Sieverts apparatus. The thermodynamic properties were determined by van't Hoff method. Due to sluggish kinetics and a highly sloped plateau, the hydriding thermodynamics could only be extracted by measuring the full PCT curves at 654 K and 664 K for the van't Hoff analysis.

Machine learning

Training Data. Our models are trained on the experimental metal-hydride thermodynamic data contained in v0.0.4 of the ML-HydPARK database,[40] which includes recent literature data on high entropy alloy hydrides[26,30,32,35,37,41] and metal hydrides for compression.[15,47] The thermodynamic quantities available in the database are hydrogen per metal saturation capacity [H/M], the ΔH [kJ/molH$_2$] and ΔS [J/(molH$_2$·K)] of the (de-)hydriding reaction, and, therefore, the Gibbs free energy or equilibrium plateau pressure at room temperature, $\ln(P^o_{eq}/P_o) = -\Delta H/(RT^o) + \Delta S/R$ (where P_o is the reference pressure of 1 bar).

Materials featurization. The Magpie strategy, as implemented in Matminer,[48] was employed for materials featurization. This strategy permits derivation of an input feature vector to an ML model using composition alone, rather than requiring an exact crystal structure which (especially for high entropy materials existing as solid solutions) is not readily defined. The set of elemental properties, p, utilized by Magpie (electronegativity, covalent radius, etc.) and the molar fractions, f, in a given composition are combined in various operations like mean ($\bar{p} = \sum_i p_i f_i$), average deviation ($\hat{p} = \sum_i f_i |p_i - \bar{p}|$), etc. While Magpie comprehensively covers standard elemental properties, we also include domain-specific features by supplementing p with ΔH_b, each element's binary hydride formation enthalpies, which we obtained from computed entries in Materials Project[49] since this value may not be experimentally accessible for non-hydriding elements.

Model training and validation. Gradient boosting tree regressors (GBR) and classifiers (GBC) have previously been found to be high-performing models for predicting hydride thermodynamics and HEA phase stability.[26] We utilized the scikit-learn[50] library's implementation of these methods to train GBR models for H/M, ΔH, ΔS, and $\ln(P^o_{eq}/P_o)$ with hyperparameters (see SI) that were tuned to minimize over-fitting by minimizing the average K-fold cross validation test set errors.[51] This average K-fold cross validation test set error is the expected model performance when predicting hydriding properties of new HEA compositions during screening.

High-throughput compositional screening. A screening set of all 4-, 5-, and 6-component equimolar high entropy compositions from the possible element set $E = \{$Mg, Al, Ti, V, Cr, Mn, Fe, Co, Ni, Cu, Zn, Zr, Nb, Mo, Pd, Hf, Ta$\}$. This yields $\binom{17}{6}+\binom{17}{5}+\binom{17}{4} =$ 20944 possible compositions. Taking the subset of what are typically considered hydriding elements, $H = \{$Mg, Ti, V, Zr, Nb, Pd, Hf, Ta$\}$, we then remove any composition whose combined molar fraction of H elements is less than 0.25 (since there are no experimental measurements in the ML-HydPARK dataset on compositions that only contain non-hydriding elements). This reduces screening space to a total of 17,920 unique equimolar compositions, and the hydriding properties of H/M, ΔH, ΔS, and/or $\ln(P^o_{eq}/P_o)$ of each composition can be predicted by the cross-validated ML models.

Pareto optimal materials Hydrogen storage materials are well-known for competing property trade-offs that hinder optimization of overall material performance, e.g., the general trade-off between gravimetric capacity and enthalpy of desorption.[3] When multiple objectives exist (that may or may not be in competition with each other), selecting optimal materials requires identifying the Pareto set, i.e. the set of materials for which no two objectives can be simultaneously improved by any other material in the dataset. For HEA hydride candidates, we seek to maximize four properties (correspond to the goal of identifying low stability, high capacity, and low material cost hydrides): (1) $-|\Delta H - 27|$, (2) H/M, (3) Hwt%, and (4) negative raw material cost. Objective 1 and 2 come directly from ML predictions, objective 3 is readily derived from objective 2, and objective 4 simply comes from tabulated elemental costs.

Code and data availability. The jupyter notebooks and data needed to reproduce this study are made publicly available (`https://github.com/mwitman1/HEAhydrideMLv2` and `https://zenodo.org/record/7324809`).

Density functional theory

Density functional theory (DFT) calculations were performed to understand the atomistic mechanisms of hydrogen absorption in selected HEA compositions. All DFT calculations were performed using the Vienna ab initio simulation package,[52] using the settings[53–56] described in the SI. For each composition (MgTiVZrNbHf, MgTiVCrNb and MgAlTiVCr), 100 body-centered cubic (BCC) random alloy configurations (3x3x2 supercells = 36 metal atoms) and 100 face-centered cubic (FCC) random alloy configurations (3x2x2 supercells = 48 metal atoms) were relaxed. For each composition and lattice type, the lowest energy structure was selected yielding E_{alloy}. For varying H/M ratios (from 0 to 2), N hydrogen atoms were inserted sequentially in tetrahedral interstitial sites (ordered from lowest to highest mean electronegativity of the surrounding metal atoms). H placement at an interstitial site was skipped if it violates an H-H minimum distance constraint (i.e., is within 1.8 Å of a previously placed hydrogen) and the hydrided structures were relaxed yielding E_{hydride}. The hydride decomposition enthalpy per mole hydrogen at 0K, ΔH_d, was then calculated as,

$$\Delta H_d(N) = \frac{1}{(N/2)}\left(E_{\text{alloy}} + \frac{N}{2}E_{\text{H}_2} - E_{\text{hydride}}\right). \quad (1)$$

Here E_{hydride} is the relaxed DFT energy of the hydrided random alloy configuration with N hydrogen atoms, E_{alloy} is the relaxed DFT energy of the same alloy configuration with no hydrogen, and E_{H_2} is the total energy of the gas-phase H_2 molecule. While ΔH_d is not the same quantity as the experimentally measured desorption enthalpy, it provides a proxy that is tractably calculated with DFT and qualitatively comparable with experimentally observed trends in HEA hydride stability.

Results and discussion

The materials discovery workflow and corresponding results are structured as follows: (1) ML models for hydride thermodynamics are

trained and their predictive capabilities assessed by comprehensive cross-validation; (2) interpretability methods are applied to these ML models to elucidate competing structure-property relationships in optimal material design; (3) HEA hydride properties are predicted and screened in high-throughput; (4) Pareto optimal HEA hydride candidates are identified as validation targets; (5) experimental synthesis, characterization, and testing confirms high-performance of predicted targets; and (6) first-principles calculations corroborate the experimentally-observed and ML-predicted trends in these new materials, while providing insights into the mechanism and thermodynamic driving forces for their high performance.

Validating hydride thermodynamic models

First, we perform detailed cross validation of our models to elucidate their predictive capabilities. The first through fourth rows of Figure 1 respectively summarize the ML models' performance on predicting hydride thermodynamics for the properties contained in v0.0.4 of ML-HydPARK database: H/M, ΔH, ΔS and $\ln\left(P^o_{eq}/P_o\right)$. Figure 1a shows parity plots for the test set predictions from a random K=10-fold cross validation split across the entire dataset. For each thermodynamic property model, the expected mean absolute error (MAE) of predictions on unseen compositions is assessed by the average MAE across all K=10 test sets, $\langle \text{MAE} \rangle_K$ and shown in Table 1. For each model, the average coefficient of determination, R^2, across all 10 test sets is also shown.

Table 1: MAE and R^2 averaged across K=10-fold test sets for H/M, ΔH [kJ/molH_2], ΔS [J/(molH_2·K)], and $\ln\left(P^o_{eq}/P_o\right)$ models.

Model	H/M	ΔH	ΔS	$\ln\left(P^o_{eq}/P_o\right)$
$\langle \text{MAE} \rangle_K$	0.14	5.4	13	1.5
$\langle R^2 \rangle_K$	0.80	0.87	0.67	0.89

Figure 1b breaks down the K-fold test set errors against the underlying data distribution. Higher accuracy is directly correlated with the density of training data for a given target property; thus, the highly non-uniform distribution of all measured properties in ML-HydPARK presents a challenge but also a significant opportunity for model improvement with the collection of additional data. The challenge is most pronounced when predicting materials at the extrema of the property ranges. For example, there are few hydrogen storage applications where one would not want to maximize H/M, but the lack of data for H/M ≥ 2 challenges predictions in this regime. Another example is the low density of training data for $\Delta H < \sim$20 kJ/molH_2, which is the typical region in which promising materials for hydrogen compression are found. Nonetheless, the models are sufficiently accurate that we can high-throughput screen HEA compositions for primary down-selection of hydrides that should be prioritized for experimental testing. Furthermore, we anticipate model accuracy will continue to improve as more experimental data is collected and as recent advancements begin to more rigorously deal with data imbalance in the context of regression (as opposed to the more developed solutions for classification).[57]

Model interpretability and competing structure-property relationships

Interpretability of ML models can critically discern underlying feature-property relationships, and reveal how materials can be rationally modified to tune a desired property. For example, the goal of SHapely Additive Predictions (SHAP)[43] is to compute the contribution, or SHAP value, of each feature to a model's prediction of a particular instance (i.e., alloy composition in this study). The SHAP analysis summary plot for each model, shown in Figure 1c, simultaneously reveals overall feature importance and feature effects. For each possible input feature (listed on the y-axis), points represent all instances in the dataset with their SHAP values on the x-axis and color-coded by the feature value. Thus, overall feature importance can be ranked by the sum of the absolute SHAP values per feature; more importantly, feature effects (i.e., SHAP values' dependence

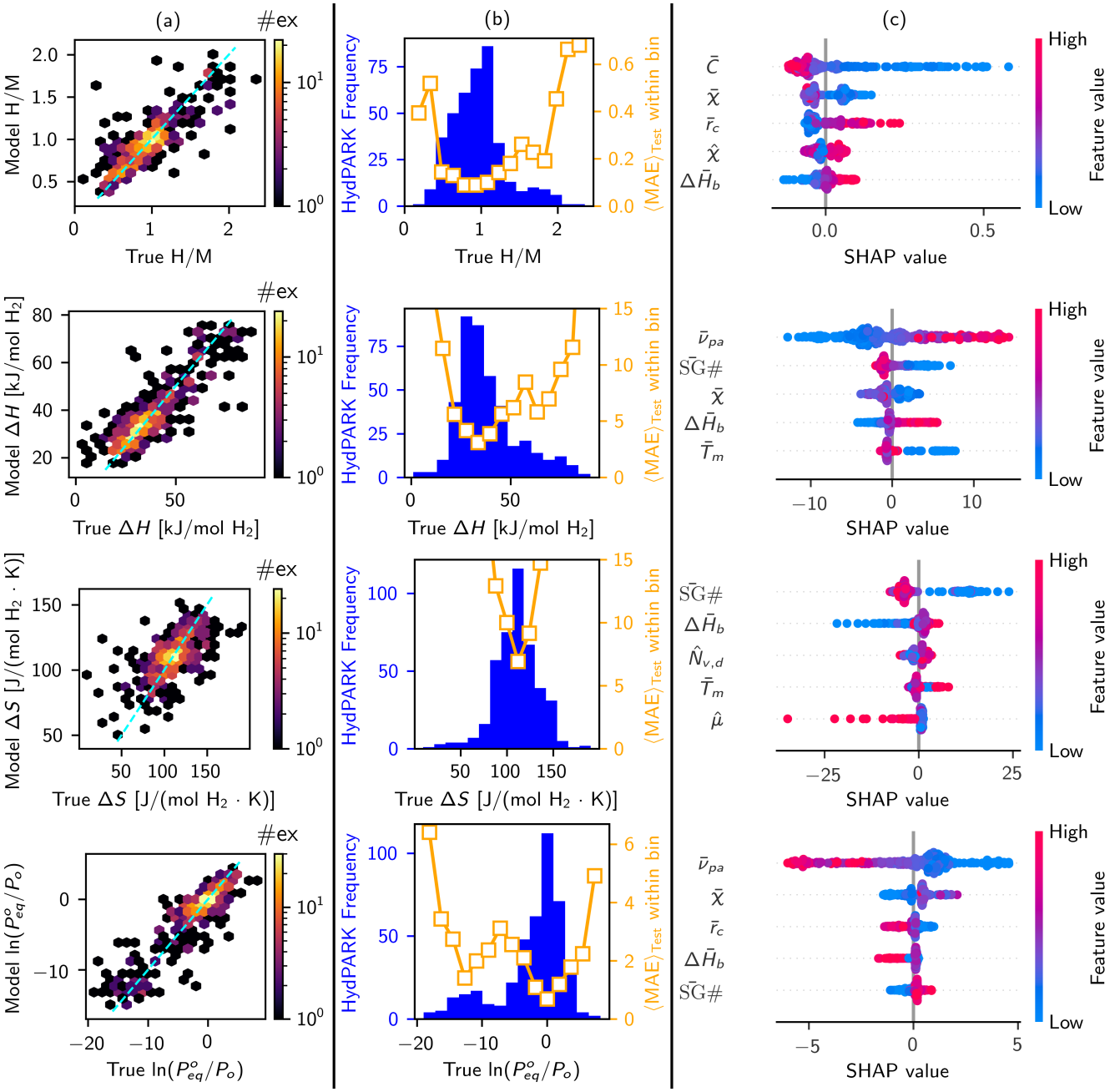

Figure 1: Column (a) shows the test set parity plots for all K=10-fold cross validation models. Color-coding corresponding to the density of training examples. Column (b) shows the histogram of the training data (blue), where test set MAEs have been plotted within an individual histogram bin (orange). The first, second, third, and fourth rows correspond to the models for H/M, ΔH, ΔS, and $\ln P^o_{eq}$, respectively. Column (c) shows the SHAP values for each feature of each hydride in the training dataset. The following appear as one of the five most important features in any given model: $\nu_{pa} \equiv$ volume per atom of elemental solid, $C \equiv$ column number, $\chi \equiv$ Pauling electronegativity, $r_c \equiv$ covalent radius, $\Delta H_b \equiv$ binary hydride formation enthalpy, $N_v \equiv$ valence electron number, $N_{v,d} \equiv$ d-valence electron number, $SG\# \equiv$ space group number of the elemental solid, $T_m \equiv$ melting temperature).

on the feature values) allows for interpretable material design rules to be extracted.

For example, the dominant feature contribution to ΔH, and hence $\ln\left(P^o_{eq}/P_o\right)$, arises from a strong correlation with $\bar{\nu}_{pa}$, or the compositionally-weighted, mean volume per

atom of the elemental solids.[22] Thus a simple, first-order design rule to tune the stability of metal hydrides can be discerned: reduce $\bar{\nu}_{pa}$ of the alloy composition to reduce hydride stability. An equally important observation is that models for different thermodynamic properties have significant overlap in the 5 globally most important features *and* share similar feature effects (SHAP values' dependence on feature values). We can therefore capture the interconnected feature-property relationships that generally hinder one's ability to independently tune the desired thermodynamic properties of metal hydrides. For example, ΔH's dependence on $\Delta\bar{H}_b$ and $\bar{\text{SG}}$# are qualitatively similar to ΔS's, indicative of the enthalpy/entropy compensation effect that generally constrains materials design.[25,58] The similar feature dependencies of the H/M and ΔH models (e.g., SHAP values for mean electronegativity, $\bar{\chi}$, and mean binary hydride formation enthalpies, $\Delta\bar{H}_b$) indicate the limited ability to independently tune hydride stability and capacity, a critical optimization problem that must be overcome, as discussed next.

Screening for Pareto optimal HEAs.

The hydriding thermodynamic properties were predicted for the selected screening space of 17,920 unique equimolar compositions. The predicted log equilibrium plateau pressures, plotted as a function of the most important ML feature, $\bar{\nu}_{pa}$, span many orders of magnitude across the HEA screening set (Figure 2a). This emphasizes the attractiveness of HEAs as a materials platform for hydrogen applications since they generally support continuous tuning of properties via expansive possibilities for chemical substitution and compositional modification.

The thermodynamic favorability of the hydriding reaction is closely correlated with saturation capacity in materials-based hydrogen storage: the stronger a material absorbs hydrogen, the higher its capacity. This correlation is detrimental to most practical applications which require high gravimetric and/or volumetric capacity (e.g., vehicular and stationary storage) but relatively low ΔH (on the order of 27 kJ/molH_2) to achieve hydrogen release without excessive heating requirements. This fundamental trade-off is clearly captured in the HEA hydride predictions shown in Figure 2b. Here we plot the absolute deviation of ΔH from a desired target enthalpy, in this case $|\Delta H - 27|$ kJ/molH_2, versus the predicted saturation capacity in terms of H/M. In the presence of these competing objectives, the Pareto front is the set of materials for which both objectives cannot be simultaneously improved by any other material in the dataset. Figure 2b shows a 4 dimensional Pareto front based on additional objectives, such as minimizing estimated raw material cost (USD/kg) and maximizing gravimetric saturation capacity, Hwt.% (as derived from predicted H/M and the molar mass of the composition). Finally, Figure 2c shows the iterative evolution of the Pareto front as previous Pareto front materials are removed from the screening dataset.

For experimental validation we chose materials that were lying on or near the Pareto front, similar to previous successful HEA hydrides, and/or had a high ratio of predicted H/M to formula weight (i.e., high gravimetric capacity for its H/M ratio). The materials selected for experimental testing in this study include MgTiVZrNbHf, MgTiVCrNb, and MgAlTiVCr. Another interesting Pareto front material is the low-cost, low-weight MgTiCrMn. Although the composition is predicted to be capable of forming a solid solution mixture using a gradient boosting classifier that essentially reproduces the Hume-Rothery rules,[26,59] our experimental efforts to synthesize a pure BCC or FCC HEA phase were not successful. However, many other interesting materials lying along the Pareto front can and should be tested in future studies. MgTiCrMnFe, for example, contains no high raw metal costs and has relatively low predicted $\Delta H = 30$ kJ/molH_2 with relatively high capacity of H/M = 1 and Hwt.% = 2.1.

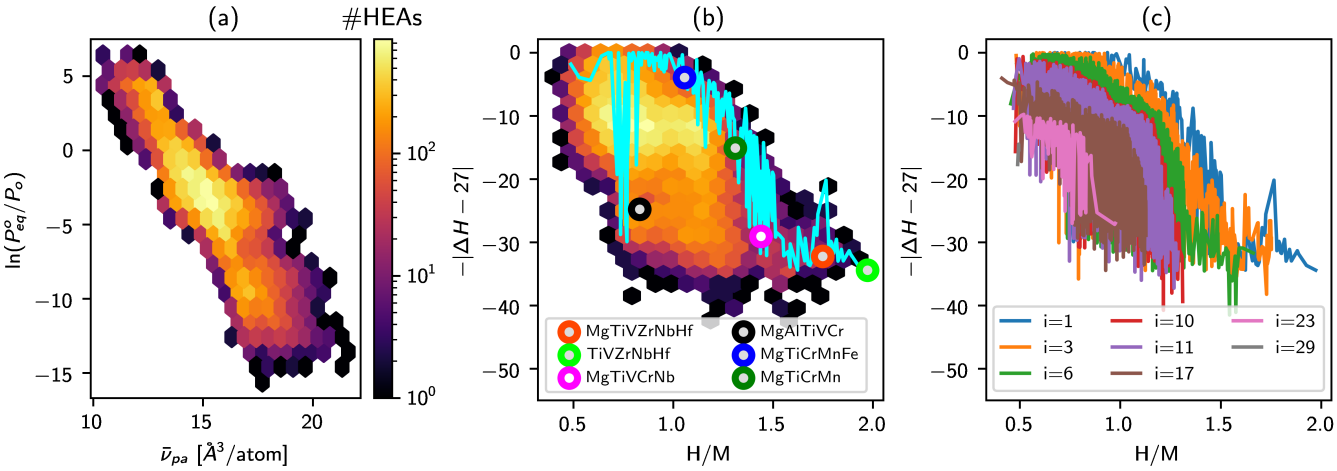

Figure 2: (a) Screening of 17,920 unique equimolar HEA compositions for predicted equilibrium plateau pressure plotted vs. the primary feature for this model, $\bar{\nu}_{pa}$, where the color coding demonstrates the density of candidate materials in that space. (b) The 4 dimensional Pareto front (cyan line) that maximizes $-|\Delta H - 27|$, H/M, Hwt.%, and negative raw material cost is projected onto a 2 dimensional plot using the same density coloring as (a). Various HEAs of interest are shown with special markers. (c) Evolution of the i^{th} Pareto front when all materials in the $i-1^{th}$ Pareto front materials have been removed.

Synthesizing, characterizing, and testing HEA hydrides

The three selected compositions MgTiVZrNbHf, MgAlTiVCr and MgTiVCrNb were successfully prepared by a two-step method mainly due to the Mg high vapour pressure that hinders the use of high temperature melting technique. The RBM technique under high H_2 pressure permits direct production of hydride phases of these compositions with high hydrogen content: 1.6, 1.34 and 1.85 H/M for MgTiVZrNbHf, MgAlTiVCr and MgTiVCrNb, respectively. The crystalline lattice of the obtained hydrides phases is FCC ($Fm\bar{3}m$) as shown in Figure 3, typical for full hydrides of BCC high entropy alloys. The lattice parameters of the FCC hydrides are 4.612(2) Å, 4.464(5) Å, and 4.297(2) Å for MgTiVZrNbHf, MgTiVCrNb, and MgAlTiVCr, respectively. A small amount of secondary amorphous phase (possibly poorly crystalline BCC phase) can be noticed at 2θ around 40^o for the composition MgAlTiVCr. This might explain the lowest hydrogen capacity of this phase relative to the other compositions and is consistent with slight and small Al enrichment zones observed by EDS (Figure 3). It is worth mentioning that hydrogen can be desorbed from these initial hydrides by heating to 450 ^{o}C under secondary vacuum and the desorbed phases adopt a BCC lattice ($Im\bar{3}m$), as expected for these materials (see TDS measurements and XRD patterns of the BCC phases after desorption in the SI).

EDS maps before and after H_2 cycling are also shown in Figure 3. Polished surfaces were not possible due to powder form of the HEAs upon hydrogenation; regardless, no phase segregration was noticeable in the EDS maps for any of the compositions. EDS spectra supporting near-equimolar elemental compositions are shown in the SI. The bottom of Figure 3 shows PCT curves for each composition, with an inset corresponding to the van't Hoff analysis from which thermodynamic parameters can be derived. Table 2 summarizes the ML predictions vs. experiment for the Pareto axis quantities (ΔH, H/M) visualized in Figure 2.

ML performance on Mg-based HEA hydrides

The ML model predicts a ΔH ranking of MgTiVZrNbHf > MgTiVCrNb > MgAlTiVCr. The significant destabilization of MgAlTiVCr relative to MgTiVZrNbHf is correctly predicted

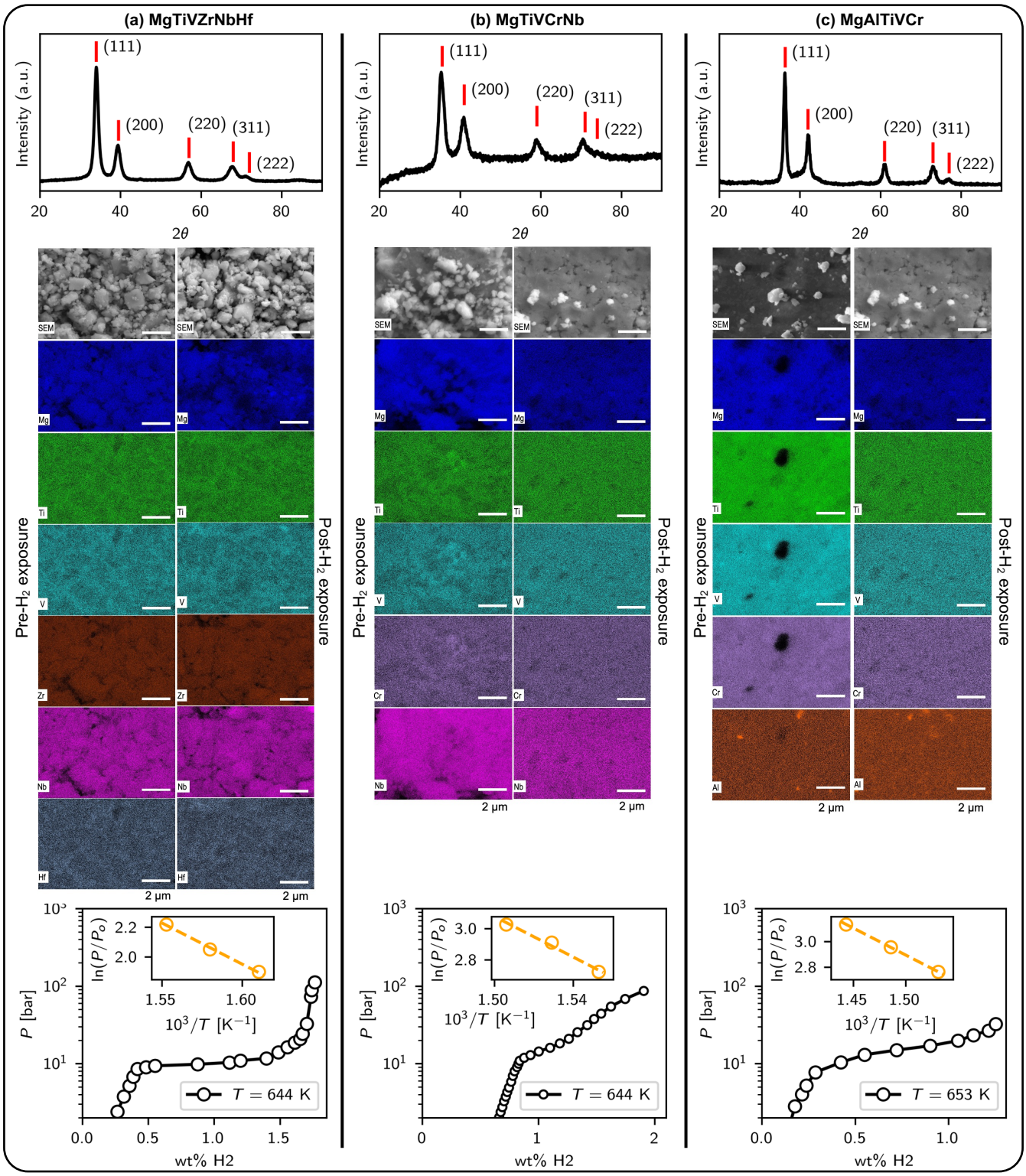

Figure 3: Experimental characterization of HEA hydrides based on MgTiVZrNbHf (left column), MgTiVCrNb (middle column), and MgAlTiVCr (right column). For each material, XRD of the RBM synthesized FCC hydride (top), EDS maps of hydrided and desorbed samples (middle), and PCT curves (bottom) and van't Hoff analysis (bottom inset) are shown.

as well as the directional effect on ΔH by Mg addition to the AlTiVCr and TiVZrNbHf parent alloys (Table 2). The ML model's ΔH predictions have the highest discrepancy with the MgTiVCrNb experiment. Yet experimental uncertainty is high ($\Delta H = 68 \pm 9$ kJ/molH_2) due the highly sloped plateau of this sample and limited range of temperature where the PCT isotherms could be collected. Furthermore, if one performs a van't Hoff analysis using only the two highest temperature and two lowest temperature PCT curves, one obtains widely varying ΔH predictions of 52 or 82 kJ/molH_2, which are below and above the ML prediction, respectively. This highlights the difficulty of extracting thermodynamic parameters when PCT curves are highly sloped and the measurement temperature range limited (see SI).

The experimental H/M saturation capacity was extracted from the last PCT measurement point for each sample. This value slightly underestimates the true saturation capacity of MgAlTiVCr and MgTiVCrNb, neither of which could be saturated at the elevated temperatures needed to ensure kinetics were fast enough to produce equilibrated PCT measurements in a reasonable amount of time. Nonetheless, all ML predictions are in reasonable quantitative agreement with experiment and correctly capture the directional change in H/M with Mg's addition in the parent alloy. Even better quantitative agreement should exist between MgAlTiVCr and MgTiVCrNb predictions and experiment, given that the true saturation capacity is higher than the maximum capacity observed in the non-saturated PCT measurements.

Hydriding mechanism and stability trends from DFT

Mechanistic insight into the thermodynamic driving force for HEAs' BCC alloy to FCC hydride transitions can be discerned from DFT calculations, and therefore used to predict hydride stability trends as a function of composition to corroborate with machine learning predictions or experiments. The hydride decomposition enthalpy per mole hydrogen at 0K, ΔH_d, was computed (see Methods and Equation (1)) for each synthesized composition in both BCC and FCC lattices and as a function of H/M, as shown in Figure 4. Generally we observe that ΔH_d of MgTiVZrNbHf > MgTiVNbCr > MgAlTiVCr. This is in good qualitative agreement with the ML model predictions and experimental PCT measurements of ΔH for MgTiVZrNbHf and MgAlTiVCr (57 and 44 kJ/molH_2, respectively). Our DFT results also indicate that at higher hydrogen loading, the ΔH_d of the FCC hydride is generally higher than that of the BCC hydride for all three compositions. This again is in good qualitative agreement with the experimentally observed BCC alloy $\rightarrow$ FCC hydride transition for all three HEA compositions, confirming the hydrogenation enthalpy is the driving force. For the two hydrides with the highest experimental capacities that approach H/M = 2 (MgTiVZrNbHf and MgTiVNbCr), the FCC ΔH_d is non-monotonic as a function of H/M, which further increases as H/M approaches 2. Meanwhile for the lowest capacity phase (MgAlTiVCr), the FCC ΔH_d is monotonically decreasing.

Interestingly, we find that for the most stable alloy configurations of all three compositions, the initial BCC alloy configurations remain as BCC after DFT structural optimizations, and the initial FCC alloy configurations transform into BCC after DFT structural optimizations, which implies the intrinsic instability of FCC alloy structures. On the other hand, for the hydrides of each alloy composition, the initial BCC hydrides undergo significant structural relaxations and no space group symmetry can be identified from the optimised structures, while the initial FCC hydrides remain as FCC after DFT structural optimizations. In summary, for selected candidate materials, DFT calculations can (1) unravel the thermodynamic driving force for the high H/M ratios observed in some of these materials, (2) reveal the driving force for the BCC $\rightarrow$ FCC phase transition, and (3) confirm the hydride stability trends as predicted by ML and observed experimentally.

Table 2: ML-predicted vs experimental values extracted from PCT curves for ΔH [kJ/molH$_2$] and saturation capacity (H/M) for HEAs tested in this work. RBM as-synthesized H/M are shown for comparison. Experimental uncertainties are computed from the linear regression in the van't Hoff analysis under the assumption of residual normality. †Non-Mg containing analogs from previous literature[26,30,37] existed in the training data for this study (i.e., they correspond to training rather than test set predictions). ‡True saturation capacity is underestimated due to incomplete saturation at the high temperatures that were needed for PCT measurements.

HEA	ΔH_{ML}	ΔH_{PCT}	H/M$_{\mathrm{ML}}$	H/M$_{\mathrm{PCT}}$	H/M$_{\mathrm{RBM}}$
TiVZrNbHf†	61	62	2.0	2.1	-
MgTiVZrNbHf	59	57 ± 4	1.5	1.8	1.6
TiVCrNb†	47	49	1.8	1.9	-
MgTiVCrNb	55	68 ± 9	1.5	1.1‡	1.85
AlTiVCr†	41	42	0.57	0.49	-
MgAlTiVCr	51	44 ± 0.2	0.83	0.51‡	1.34

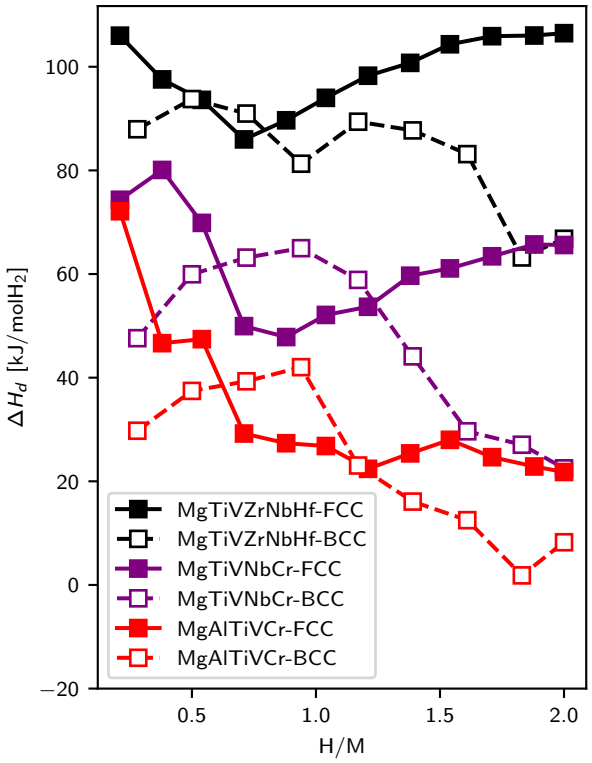

Figure 4: DFT-computed hydride decomposition enthalpy (at 0 K) for random alloy configurations as a function of H/M for the three HEAs synthesized in this work. For each composition, the decomposition enthalpy was calculated for both the FCC and BCC lattices.

Conclusions

High entropy alloys and their hydrides present an intractably large compositional design space for experiments or costly first-principles calculations like DFT, so efficient data-driven models that (1) capture key materials descriptors and (2) can predict primary thermodynamic evaluation criteria are critical. We have demonstrated how explainable machine learning models capture the dependence of different thermodynamic properties (e.g., ΔH, ΔS, or H/M) on the same critical materials features, which in turn generally produces unavoidable trade-offs in desired hydride thermodynamic properties. These include enthalpy-entropy compensation (e.g., positive correlations in ΔH vs. ΔS) as well as the capacity-enthalpy trade-off (e.g., H/M vs. ΔH) in the design of optimal materials. When high-throughput screening is performed on novel HEA hydride compositions, such trade-offs are explicitly captured and the selection of optimal materials can be re-framed as a Pareto optimal selection task. In this work we selected various Mg-containing HEAs that were predicted to be on or near the Pareto front for experimental synthesis and validation, and good agreement was obtained between ML predictions, DFT analysis, and experiments. Sacrificing capacity for decreased ΔH was unavoidable in these selected materials, which clearly highlights the need for predicting and further synthesizing Pareto efficient materials.

Moving forward, significant work remains on both computational and experimental fronts. For example, an ability to directly model the PCT curves of a proposed HEA with DFT-level accuracy would provide a step-change improve-

ment in the predictive capabilities and better direct experimental efforts. The continued acquisition and integration of literature experiments into the training data will be paramount for continued improvement of the compositional model, especially in property space with low amounts of data. Furthermore, databases of hydrogen absorption/desorption kinetics need to be assembled so that this quantity can be added to the multi-objective Pareto front. On the experimental front, higher-throughput efforts to obtain metal hydride thermodynamics (e.g., using high-pressure calorimetry methods) could further accelerate the validation of Pareto optimal hydrides, provide more data for improved ML models, and even allow active learning feedback loops between ML and experiment for optimal materials design.

Author Contributions

Conceptualization, M.D.W., M.D.A., and V.S.; Methodology, Software, and Validation, M.W., S.L.; Formal Analyses and Investigation, M.D.W., S.L., M.Wadge, A.B., N.P-R., R.C., G.E., J.C., E.J.A., and V.S.; Data Curation, M.D.W.; Funding Acquisition, S.L., S.A., M.D.A., G.S.W., D.M.G., M.S., C.Z., and V.S.; Writing - Original Draft Preparation, M.D.W., S.L., C.Z., M.S., and V.S.; Writing - Review & Editing, All authors.

Conflicts of Interest

There are no conflicts to declare.

Acknowledgements

The authors gratefully acknowledge research support from the U.S. Department of Energy, Office of Energy Efficiency and Renewable Energy, Hydrogen and Fuel Cell Technologies Office through the Hydrogen Storage Materials Advanced Research Consortium (HyMARC). This work was supported by the Laboratory Directed Research and Development (LDRD) program at Sandia National Laboratories. Sandia National Laboratories is a multi-mission laboratory managed and operated by National Technology & Engineering Solutions of Sandia, LLC (NTESS), a wholly owned subsidiary of Honeywell International Inc., for the U.S. Department of Energy's National Nuclear Security Administration (DOE/NNSA) under contract DE-NA0003525. This written work is authored by an employee of NTESS. The employee, not NTESS, owns the right, title and interest in and to the written work and is responsible for its contents. Any subjective views or opinions that might be expressed in the written work do not necessarily represent the views of the U.S. Government. The publisher acknowledges that the U.S. Government retains a non-exclusive, paid-up, irrevocable, world-wide license to publish or reproduce the published form of this written work or allow others to do so, for U.S. Government purposes. The DOE will provide public access to results of federally sponsored research in accordance with the DOE Public Access Plan. G.E and M.S acknowledge funding from NordForsk through the project "Neutrons for multi-functional hydrides – FunHy" (project Nr. 81492). Work at the University of Nottingham is supported by EPSRC (EP/V042556/1, EP/P020232/1, and EP/R029431/1). We acknowledge the use of the Athena supercomputer through the HPC Midlands+ Consortium, and the ARCHER supercomputer through membership of the UK's HPC Materials Chemistry Consortium, which are funded by EPSRC Grants No. EP/P020232/1 and No. EP/R029431/1, respectively.

References

(1) Wu, D.; Wang, D.; Ramachandran, T.; Holladay, J. A techno-economic assessment framework for hydrogen energy storage toward multiple energy delivery pathways and grid services. *Energy* **2022**, *249*, 123638.

(2) Schlapbach, L.; Züttel, A. Hydrogen-

storage materials for mobile applications. *Nature* **2001**, *414*, 353–358.

(3) Allendorf, M. D.; Stavila, V.; Snider, J. L.; Witman, M.; Bowden, M. E.; Brooks, K.; Tran, B. L.; Autrey, T. Challenges to developing materials for the transport and storage of hydrogen. *Nat. Chem.* **2022**,

(4) Reilly, J. J.; Wiswall, R. H. Reaction of hydrogen with alloys of magnesium and nickel and the formation of Mg_2NiH_4. *Inorg. Chem.* **1968**, *7*, 2254–2256.

(5) Reilly, J. J.; Wiswall, R. H. Formation and properties of iron titanium hydride. *Inorg. Chem.* **1974**, *13*, 218–222.

(6) Reilly, J. Chemistry of Intermetallic Hydrides. 180th Meet. Electrochem. Soc. 1991.

(7) Vajo, J. J.; Mertens, F.; Ahn, C. C.; Bowman, R. C.; Fultz, B. Altering Hydrogen Storage Properties by Hydride Destabilization through Alloy Formation: LiH and MgH_2 Destabilized with Si. *J. Phys. Chem. B* **2004**, *108*, 13977–13983.

(8) Wang, P.; Jensen, C. Method for preparing Ti-doped NaAlH4 using Ti powder: observation of an unusual reversible dehydrogenation behavior. *J. Alloys Compd.* **2004**, *379*, 99–102.

(9) Alapati, S. V.; Johnson, J. K.; Sholl, D. S. Identification of Destabilized Metal Hydrides for Hydrogen Storage Using First Principles Calculations. *J. Phys. Chem. B* **2006**, *110*, 8769–8776.

(10) Walker, G. S.; Abbas, M.; Grant, D. M.; Udeh, C. Destabilisation of magnesium hydride by germanium as a new potential multicomponent hydrogen storage system. *Chem. Commun.* **2011**, *47*, 8001.

(11) Pasquini, L. et al. Magnesium- and intermetallic alloys-based hydrides for energy storage: modelling, synthesis and properties. *Prog. Energy* **2022**, *4*, 032007.

(12) Orimo, S.-i.; Nakamori, Y.; Eliseo, J. R.; Züttel, A.; Jensen, C. M. Complex Hydrides for Hydrogen Storage. *Chem. Rev.* **2007**, *107*, 4111–4132.

(13) Milanese, C.; Jensen, T.; Hauback, B.; Pistidda, C.; Dornheim, M.; Yang, H.; Lombardo, L.; Zuettel, A.; Filinchuk, Y.; Ngene, P.; de Jongh, P.; Buckley, C.; Dematteis, E.; Baricco, M. Complex hydrides for energy storage. *Int. J. Hydrogen Energy* **2019**, *44*, 7860–7874.

(14) Züttel, A.; Remhof, A.; Borgschulte, A.; Friedrichs, O. Hydrogen: the future energy carrier. *Philos. Trans. R. Soc. A Math. Phys. Eng. Sci.* **2010**, *368*, 3329–3342.

(15) Lototskyy, M.; Yartys, V.; Pollet, B.; Bowman, R. Metal hydride hydrogen compressors: A review. *Int. J. Hydrogen Energy* **2014**, *39*, 5818–5851.

(16) Yartys, V. A.; Lototskyy, M.; Linkov, V.; Grant, D.; Stuart, A.; Eriksen, J.; Denys, R.; Bowman, R. C. Metal hydride hydrogen compression: recent advances and future prospects. *Appl. Phys. A* **2016**, *122*, 415.

(17) Dornheim, M. et al. Research and development of hydrogen carrier based solutions for hydrogen compression and storage. *Prog. Energy* **2022**, *4*, 042005.

(18) Dornheim, M. *Thermodyn. - Interact. Stud. - Solids, Liq. Gases*; InTech, 2011.

(19) Hutcheon, M. J.; Shipley, A. M.; Needs, R. J. Predicting novel superconducting hydrides using machine learning approaches. *Phys. Rev. B* **2020**, *101*, 144505.

(20) Wang, S.; Wu, Z.; Dai, S.; Jiang, D. Deep Learning Accelerated Determination of Hydride Locations in Metal Nanoclusters. *Angew. Chemie Int. Ed.* **2021**, *60*, 12289–12292.

(21) Hattrick-Simpers, J. R.; Choudhary, K.; Corgnale, C. A simple constrained machine learning model for predicting high-pressure-hydrogen-compressor materials. *Mol. Syst. Des. Eng.* **2018**, *3*, 509–517.

(22) Ward, L.; Agrawal, A.; Choudhary, A.; Wolverton, C. A general-purpose machine learning framework for predicting properties of inorganic materials. *npj Comput. Mater.* **2016**, *2*, 16028.

(23) Goodall, R. E. A.; Lee, A. A. Predicting materials properties without crystal structure: deep representation learning from stoichiometry. *Nat. Commun.* **2020**, *11*, 6280.

(24) Bartel, C. J.; Trewartha, A.; Wang, Q.; Dunn, A.; Jain, A.; Ceder, G. A critical examination of compound stability predictions from machine-learned formation energies. *npj Comput. Mater.* **2020**, *6*, 97.

(25) Witman, M.; Ling, S.; Grant, D. M.; Walker, G. S.; Agarwal, S.; Stavila, V.; Allendorf, M. D. Extracting an Empirical Intermetallic Hydride Design Principle from Limited Data via Interpretable Machine Learning. *J. Phys. Chem. Lett.* **2020**, *11*, 40–47.

(26) Witman, M.; Ek, G.; Ling, S.; Chames, J.; Agarwal, S.; Wong, J.; Allendorf, M. D.; Sahlberg, M.; Stavila, V. Data-Driven Discovery and Synthesis of High Entropy Alloy Hydrides with Targeted Thermodynamic Stability. *Chem. Mater.* **2021**, *33*, 4067–4076.

(27) Miracle, D.; Senkov, O. A critical review of high entropy alloys and related concepts. *Acta Mater.* **2017**, *122*, 448–511.

(28) Senkov, O. N.; Miller, J. D.; Miracle, D. B.; Woodward, C. Accelerated exploration of multi-principal element alloys with solid solution phases. *Nat. Commun.* **2015**, *6*, 1–10.

(29) Marques, F.; Balcerzak, M.; Winkelmann, F.; Zepon, G.; Felderhoff, M. Review and outlook on high-entropy alloys for hydrogen storage. *Energy Environ. Sci.* **2021**,

(30) Sahlberg, M.; Karlsson, D.; Zlotea, C.; Jansson, U. Superior hydrogen storage in high entropy alloys. *Sci. Rep.* **2016**, *6*, 36770.

(31) Chaudhary, V.; Chaudhary, R.; Banerjee, R.; Ramanujan, R. Accelerated and conventional development of magnetic high entropy alloys. *Mater. Today* **2021**, *49*, 231–252.

(32) Pineda-Romero, N.; Witman, M.; Stavila, V.; Zlotea, C. The effect of 10 at.% Al addition on the hydrogen storage properties of the Ti0.33V0.33Nb0.33 multi-principal element alloy. *Intermetallics* **2022**, *146*, 107590.

(33) Montero, J.; Zlotea, C.; Ek, G.; Crivello, J.-C.; Laversenne, L.; Sahlberg, M. TiVZrNb Multi-Principal-Element Alloy: Synthesis Optimization, Structural, and Hydrogen Sorption Properties. *Molecules* **2019**, *24*, 2799.

(34) Nygård, M. M.; Ek, G.; Karlsson, D.; Sørby, M. H.; Sahlberg, M.; Hauback, B. C. Counting electrons - A new approach to tailor the hydrogen sorption properties of high-entropy alloys. *Acta Mater.* **2019**, *175*, 121–129.

(35) Ek, G.; Nygård, M. M.; Pavan, A. F.; Montero, J.; Henry, P. F.; Sørby, M. H.; Witman, M.; Stavila, V.; Zlotea, C.; Hauback, B. C.; Sahlberg, M. Elucidating the Effects of the Composition on Hydrogen Sorption in TiVZrNbHf-Based High-Entropy Alloys. *Inorg. Chem.* **2021**, *60*, 1124–1132.

(36) Edalati, P.; Floriano, R.; Mohammadi, A.; Li, Y.; Zepon, G.; Li, H.-W.; Edalati, K. Reversible room temperature hydrogen storage in high-entropy alloy TiZrCrMnFeNi. *Scr. Mater.* **2020**, *178*, 387–390.

(37) Nygård, M. M.; Fjellvåg, Ø. S.; Sørby, M. H.; Sakaki, K.; Ikeda, K.; Armstrong, J.; Vajeeston, P.; Sławiński, W. A.; Kim, H.; Machida, A.; Nakamura, Y.; Hauback, B. C. The average and local structure of $TiVCrNbD_x$ (x=0;2:2;8) from total scattering and neutron spectroscopy. *Acta Mater.* **2021**, *205*, 116496.

(38) Montero, J.; Ek, G.; Sahlberg, M.; Zlotea, C. Improving the hydrogen cycling properties by Mg addition in Ti-V-Zr-Nb refractory high entropy alloy. *Scr. Mater.* **2021**, *194*, 113699.

(39) Cardoso, K. R.; Roche, V.; Jorge Jr, A. M.; Antiqueira, F. J.; Zepon, G.; Champion, Y. Hydrogen storage in MgAlTiFeNi high entropy alloy. *J. Alloys Compd.* **2021**, *858*, 158357.

(40) Witman, M.; Allendorf, M.; Stavila, V. Database for machine learning of hydrogen stroge materials properties (0.0.4) [Data set]. 2022; `https://doi.org/10.5281/zenodo.7293164`.

(41) Silva, B. H.; Zlotea, C.; Champion, Y.; Botta, W. J.; Zepon, G. Design of TiVNb-(Cr, Ni or Co) multicomponent alloys with the same valence electron concentration for hydrogen storage. *J. Alloys Compd.* **2021**, *865*, 158767.

(42) Lundberg, S.; Lee, S.-I. A Unified Approach to Interpreting Model Predictions. *Adv. Neural Inf. Process. Syst.* **2017**, 4766–4775.

(43) Lundberg, S. M.; Erion, G. G.; Lee, S.-I. Consistent Individualized Feature Attribution for Tree Ensembles. 2019-03-07. *arXiv:1802.03888v3* (accessed 2020–09–02).

(44) Boyce, B. L.; Uchic, M. D. Progress toward autonomous experimental systems for alloy development. *MRS Bull.* **2019**, *44*, 273–280.

(45) Zhou, C.; Gao, Y.; Bowman, R. C.; Zhang, J.; Liu, H.; Sun, P.; Fang, Z. Z. A high throughput dynamic method for characterizing thermodynamic properties of catalyzed magnesium hydrides by thermogravimetric analysis. *Phys. Chem. Chem. Phys.* **2021**, *23*, 15374–15383.

(46) Stach, E. et al. Autonomous experimentation systems for materials development: A community perspective. *Matter* **2021**, *4*, 2702–2726.

(47) Bellosta von Colbe, J. et al. Application of hydrides in hydrogen storage and compression: Achievements, outlook and perspectives. *Int. J. Hydrogen Energy* **2019**, *44*, 7780–7808.

(48) Ward, L. et al. Matminer: An open source toolkit for materials data mining. *Comput. Mater. Sci.* **2018**, *152*, 60–69.

(49) Jain, A.; Ong, S. P.; Hautier, G.; Chen, W.; Richards, W. D.; Dacek, S.; Cholia, S.; Gunter, D.; Skinner, D.; Ceder, G.; Persson, K. A. Commentary: The Materials Project: A materials genome approach to accelerating materials innovation. *APL Mater.* **2013**, *1*, 011002.

(50) Pedregosa, F. et al. Scikit-learn: Machine Learning in Python. *Journal of Machine Learning Research* **2011**, *12*, 2825–2830.

(51) Bergstra, J.; Yamins, D.; Cox, D. D. Making a science of model search: Hyperparameter optimization in hundreds of dimensions for vision architectures. 30th Int. Conf. Mach. Learn. ICML 2013. 2013; pp 115–123.

(52) Kresse, G.; Furthmüller, J. Efficient iterative schemes for ab initio total-energy calculations using a plane-wave basis set. *Phys. Rev. B* **1996**, *54*, 11169–11186.

(53) Perdew, J. P.; Burke, K.; Ernzerhof, M. Generalized Gradient Approximation Made Simple. *Phys. Rev. Lett.* **1996**, *77*, 3865–3868.

(54) Blöchl, P. E. Projector augmented-wave method. *Phys. Rev. B* **1994**, *50*, 17953–17979.

(55) Hobbs, D.; Kresse, G.; Hafner, J. Fully unconstrained noncollinear magnetism within the projector augmented-wave method. *Phys. Rev. B* **2000**, *62*, 11556–11570.

(56) Methfessel, M.; Paxton, A. T. High-precision sampling for Brillouin-zone integration in metals. *Phys. Rev. B* **1989**, *40*, 3616–3621.

(57) Yang, Y.; Zha, K.; Chen, Y.-C.; Wang, H.; Katabi, D. Delving into Deep Imbalanced Regression. Proc. 38th Int. Conf. Mach. Learn. 2021.

(58) Yartys, V. A.; Lototskyy, M. V. Laves type intermetallic compounds as hydrogen storage materials: A review. *J. Alloys Compd.* **2022**, *916*, 165219.

(59) Huang, W.; Martin, P.; Zhuang, H. L. Machine-learning phase prediction of high-entropy alloys. *Acta Mater.* **2019**, *169*, 225–236.

Supporting Information for: *Towards Pareto optimal high entropy alloy hydrides via data-driven materials discovery*

Matthew Witman*[1], Sanliang Ling[2], Matthew Wadge[2], Anis Bouzidi[3], Nayely Pineda-Romero[3], Rebecca Clulow[4], Gustav Ek[4], Jeffery Chames[1], Emily Allendorf[1], Sapan Agarwal[1], Mark Allendorf[1], Gavin S. Walker[2], David Grant[2], Martin Sahlberg[4], Claudia Zlotea[3] and Vitalie Stavila*[1]

[1]Sandia National Laboratories, Livermore, California 94551, USA
[2]Advanced Materials Research Group, Faculty of Engineering, University of Nottingham, University Park, Nottingham, NG7 2RD, UK
[3]Univ Paris Est Créteil, CNRS, ICMPE, UMR 7182, 2 rue Henri Dunant, 94320, Thiais, France
[4]Department of Chemistry - Ångström Laboratory, Uppsala University, Box 523, SE-75120, Uppsala, Sweden

S1. ML-ready HydPARK augmentation with HEA hydride thermodynamics

v0.0.4 of the ML-HydPARK database[1] was supplemented with thermodynamic properties of hydrides investigated for thermal hydrogen compression as summarized in Refs. 2 and 3, as well as the HEA hydride measurements we collected from the recent literature in Table S1. The jupyter notebook to reproduce these results is provided at `https://github.com/mwitman1/HEAhydrideMLv2`, and the scikit-learn gradient boosting regressor hyperparameters utilized were: {'n_estimators'=1500, 'learning_rate'=0.005, 'learning_rate'=0.005, 'max_depth'=4, 'subsample'=0.75, 'alpha'=0.99}.

Composition	ΔH	ΔS	$\ln\left(P^o_{eq}/P_o\right)$	Hwt.%	H/M	T	Reference
NbTiVZrHf	61.8	88.0	-14.35	2.2	2.06	315.0	Ref. 4
VTiZrNb	67.6	90.3	-16.41	1.5	1.07	311.0	Ref. 5
$NbTiV_{0.5}ZrHf$	59.1	87.4	-13.33	1.8	1.76	326.0	Ref. 5
VTiAlCr	42.7	88.4	-6.59	1.1	0.49	311.0	Ref. 6
VTiAlTaNb	56.1	92.1	-11.55	1.25	1.0	301.0	Ref. 6
TiVCrNb	47.1	122.0	-4.33	3.0	1.87	100.0	Ref. 7
$Al_{0.1}Ti_{0.3}V_{0.3}Nb_{0.3}$	48.6	154.0	-1.08	2.6	1.59	62.5	Ref. 8

Table S1: HEA hydride thermodynamic data from recent literature.

*mwitman@sandia.gov ; vnstavi@sandia.gov

S2. DFT settings

All density functional theory (DFT) calculations, including structural optimizations and total energy calculations, were performed using the Vienna Ab initio Simulation Package.[9] We used a plane-wave basis set with a kinetic energy cutoff of 400 eV to expand the wave functions, and the Perdew-Burke-Ernzerhof functional[10] with the projector augmented wave method[11,12] were used to solve the Kohn-Sham equations. A first-order Methfessel-Paxton smearing[13] with a width of 0.2 eV was used to improve the convergence of electronic self-consistent field calculations. All DFT calculations have been performed using a k-point mesh with a spacing of ca. 0.20 $Å^{-1}$. An energy convergence threshold of 10^{-4} eV was used for all total energy calculations. Due to the large number of structures that need to be considered, a relatively loose structural optimization convergence criterion was used, where the structural optimizations, including cell parameters and atomic positions, were considered converged if all interatomic forces fall below 0.05 eV/Å.

S3. H_2 desorption characterization

Hydrogen can be desorbed from the RBM synthesized FCC hydrides by heating to 450 °C under secondary vacuum, thereby demonstrating reversible reaction with hydrogen, as shown by the thermal desorption spectroscopy (TDS) measurements in Figure S1. The desorbed phases adopt a BCC lattice ($Im\bar{3}m$) in Figure S1, as expected for these materials. Peak refinement yields the lattice parameters of 3.404(5) Å, 3.155(8) Å, and 3.067(2) Å for MgTiVNbZrHf, MgTiVCrNb, and MgAlTiVCr respectively, which is consistent with the trend of FCC hydride lattice parameters in the main text. These values are compared to the DFT-relaxed BCC configurations described in the main text in Table S2. The DFT-relaxed, dihydride FCC (H/M = 2) random alloy configurations for each composition visualize slight distortions to metal and tetrahedral hydrogen locations arising from local strain induced by the random metal ordering in the HEA lattice (Figure S2).

Composition	Experiment	DFT
MgTiVNbZrHf	19.7	19.1
MgTiVCrNb	15.7	16.2
MgAlTiVCr	14.4	15.6

Table S2: Volume per atom of the experimentally resolved BCC alloys and the DFT relaxed random alloy configuration.

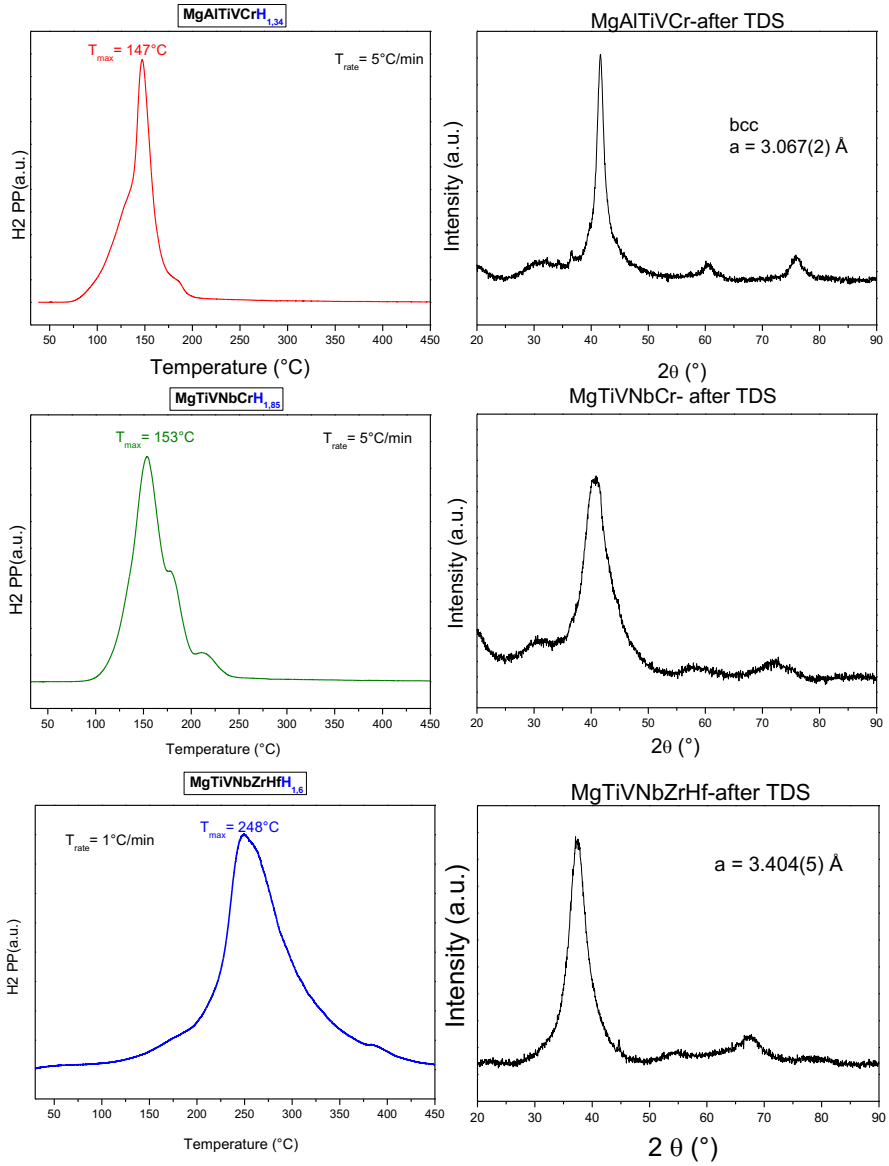

Figure S1: TDS of as synthesized FCC hydrides and XRD of the dehydrogenated BCC alloy phase.

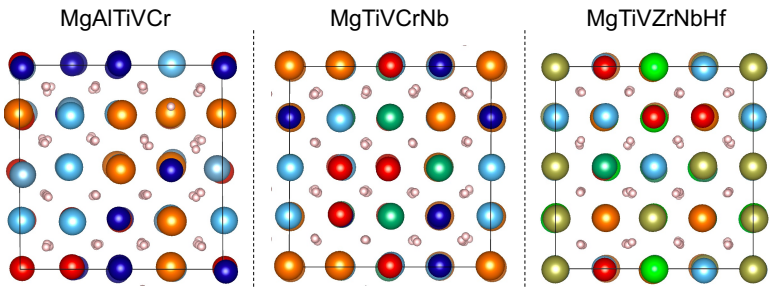

Figure S2: DFT-relaxed, dihydride (H/M = 2) FCC alloy configurations for each composition.

S4. MgTiVCrNb PCT measurements

Due to sluggish kinetics and a highly sloped plateau of MgTiVCrNb, the hydriding thermodynamics could only be extracted by measuring the full PCT curves at 644 K, 654 K and 664 K for the van't Hoff analysis, rather than the method used for MgAlTiVCr and MgTiVZrNbHf. The isotherms at each temperature and corresponding van't Hoff plot (inset) are shown in Figure S3. The experimental uncertainty in the van't Hoff analysis is high ($\Delta H = 68 \pm 9$ kJ/molH_2) due the highly sloped plateau of this sample and limited range of temperatures where the PCT isotherms could be collected. If one performs a van't Hoff analysis using only the two highest temperature and two lowest temperature PCT curves, one obtains widely varying ΔH predictions of 52 or 82 kJ/molH_2, which are below and above the ML prediction, respectively.

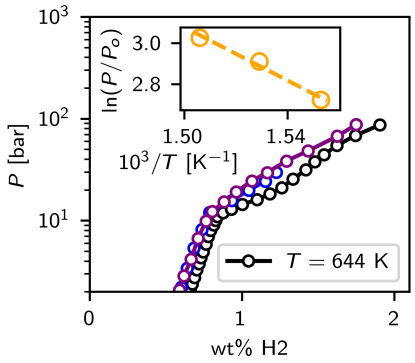

Figure S3: PCT curves for MgTiVCrNb are shown with black, blue, and purple corresponding to 644 K, 654 K, and 664 K measurements, respectively. The inset shows the pressure vs. inverse temperature points used in the van't Hoff analysis.

S5. EDS Spectra

EDS spectrum corresponding to the EDS maps in the main manuscript (after H_2 cycling) are shown in Figure S4. The EDS spectra confirm the elemental composition of the HEA samples. The small amounts of iron present are from the ball-milling hardware.

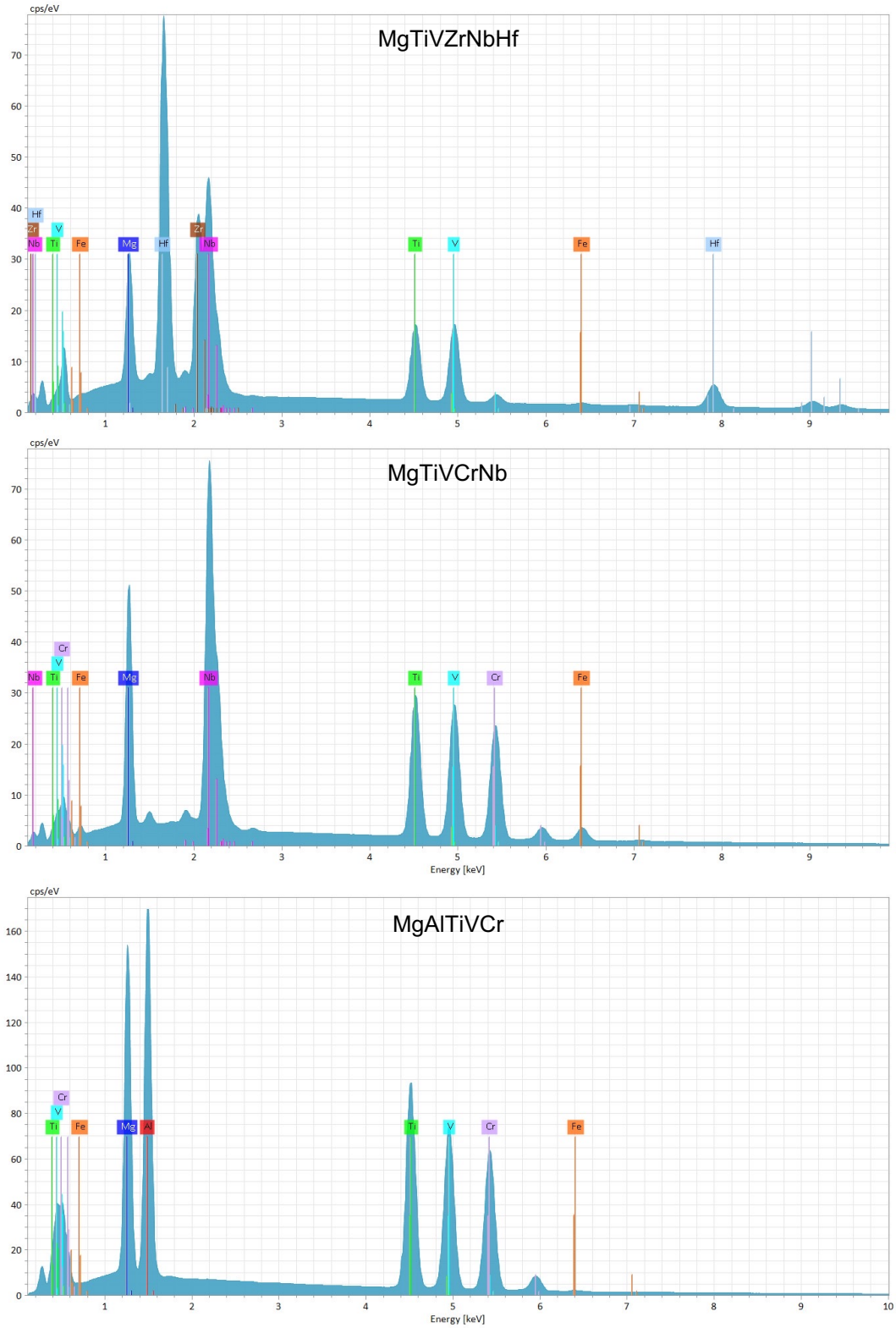

Figure S4: EDS spectra for MgTiVNbZrHf, MgTiVNbCr, and MgAlTiVCr after H_2 cycling.

References

[1] M. Witman, M. Allendorf, and V. Stavila, "Database for machine learning of hydrogen stroge materials properties (0.0.4) [Data set]," 2022.

[2] M. Lototskyy, V. Yartys, B. Pollet, and R. Bowman, "Metal hydride hydrogen compressors: A review," *Int. J. Hydrogen Energy*, vol. 39, pp. 5818–5851, apr 2014.

[3] J. Bellosta von Colbe, J.-R. Ares, J. Barale, M. Baricco, C. Buckley, G. Capurso, N. Gallandat, D. M. Grant, M. N. Guzik, I. Jacob, E. H. Jensen, T. Jensen, J. Jepsen, T. Klassen, M. V. Lototskyy, K. Manickam, A. Montone, J. Puszkiel, S. Sartori, D. A. Sheppard, A. Stuart, G. Walker, C. J. Webb, H. Yang, V. Yartys, A. Züttel, and M. Dornheim, "Application of hydrides in hydrogen storage and compression: Achievements, outlook and perspectives," *Int. J. Hydrogen Energy*, vol. 44, pp. 7780–7808, mar 2019.

[4] M. Sahlberg, D. Karlsson, C. Zlotea, and U. Jansson, "Superior hydrogen storage in high entropy alloys," *Sci. Rep.*, vol. 6, p. 36770, dec 2016.

[5] G. Ek, M. M. Nygård, A. F. Pavan, J. Montero, P. F. Henry, M. H. Sørby, M. Witman, V. Stavila, C. Zlotea, B. C. Hauback, and M. Sahlberg, "Elucidating the Effects of the Composition on Hydrogen Sorption in TiVZrNbHf-Based High-Entropy Alloys," *Inorg. Chem.*, vol. 60, pp. 1124–1132, jan 2021.

[6] M. Witman, G. Ek, S. Ling, J. Chames, S. Agarwal, J. Wong, M. D. Allendorf, M. Sahlberg, and V. Stavila, "Data-Driven Discovery and Synthesis of High Entropy Alloy Hydrides with Targeted Thermodynamic Stability," *Chem. Mater.*, vol. 33, pp. 4067–4076, jun 2021.

[7] M. M. Nygård, Ø. S. Fjellvåg, M. H. Sørby, K. Sakaki, K. Ikeda, J. Armstrong, P. Vajeeston, W. A. Sławiński, H. Kim, A. Machida, Y. Nakamura, and B. C. Hauback, "The average and local structure of $TiVCrNbD_x$ (x=0;2:2;8) from total scattering and neutron spectroscopy," *Acta Mater.*, vol. 205, p. 116496, feb 2021.

[8] N. Pineda-Romero, M. Witman, V. Stavila, and C. Zlotea, "The effect of 10 at.% Al addition on the hydrogen storage properties of the Ti0.33V0.33Nb0.33 multi-principal element alloy," *Intermetallics*, vol. 146, p. 107590, jul 2022.

[9] G. Kresse and J. Furthmüller, "Efficient iterative schemes for ab initio total-energy calculations using a plane-wave basis set," *Phys. Rev. B*, vol. 54, pp. 11169–11186, Oct. 1996.

[10] J. P. Perdew, K. Burke, and M. Ernzerhof, "Generalized gradient approximation made simple," *Phys. Rev. Lett.*, vol. 77, pp. 3865–3868, Oct. 1996.

[11] P. E. Blöchl, "Projector augmented-wave method," *Phys. Rev. B*, vol. 50, pp. 17953–17979, Dec. 1994.

[12] D. Hobbs, G. Kresse, and J. Hafner, "Fully unconstrained noncollinear magnetism within the projector augmented-wave method," *Phys. Rev. B*, vol. 62, pp. 11556–11570, Nov. 2000.

[13] M. Methfessel and A. T. Paxton, "High-precision sampling for brillouin-zone integration in metals," *Phys. Rev. B*, vol. 40, pp. 3616–3621, Aug. 1989.